



Deposited via The University of Leeds.

White Rose Research Online URL for this paper:

<https://eprints.whiterose.ac.uk/id/eprint/79741/>

Version: Accepted Version

---

**Article:**

Mao, X, Yu, Z, Jaworski, AJ et al. (2008) PIV studies of coherent structures generated at the end of a stack of parallel plates in a standing wave acoustic field. *Experiments in Fluids*, 45 (5). 833 - 846. ISSN: 0723-4864

<https://doi.org/10.1007/s00348-008-0503-7>

---

**Reuse**

Items deposited in White Rose Research Online are protected by copyright, with all rights reserved unless indicated otherwise. They may be downloaded and/or printed for private study, or other acts as permitted by national copyright laws. The publisher or other rights holders may allow further reproduction and re-use of the full text version. This is indicated by the licence information on the White Rose Research Online record for the item.

**Takedown**

If you consider content in White Rose Research Online to be in breach of UK law, please notify us by emailing [eprints@whiterose.ac.uk](mailto:eprints@whiterose.ac.uk) including the URL of the record and the reason for the withdrawal request.

# PIV studies of coherent structures generated at the end of a stack of parallel plates in a standing wave acoustic field

Xiaoan MAO, Zhibin YU, Artur J JAWORSKI<sup>1</sup> and David MARX  
School of Mechanical, Aerospace and Civil Engineering  
The University of Manchester  
Sackville Street, PO Box 88, Manchester M60 1QD, UK

## Abstract

Oscillating flow near the end of a stack of parallel plates placed in a standing wave resonator is investigated using Particle Image Velocimetry (PIV). The Reynolds number,  $Re_d$ , based on the plate thickness and the velocity amplitude at the entrance to the stack, is controlled by varying the acoustic excitation (so-called drive ratio) and by using two configurations of the stacks. As the Reynolds number changes, a range of distinct flow patterns is reported for the fluid being ejected from the stack. Symmetrical and asymmetrical vortex shedding phenomena are shown and two distinct modes of generating “vortex streets” are identified.

## 1. Introduction

Flow structures generated by steady flows past bluff bodies have been a subject of many theoretical and experimental studies, the classic example being formation of the von Karman “vortex street” behind circular cylinders (Kovasznay, 1949). This class of phenomena is important in many industrial problems including: aerospace flows, civil and marine engineering, design of heat exchangers or the behaviour of overhead power cables. Somewhat more complex situation arises when steady flows are replaced by oscillatory flows (with or without the steady component), the fundamental difference being that vortices shed in one half of the cycle impinge on the bluff body when the flow reverses and may interact with vortices shed during the other half of the cycle. This may lead to interesting “lock-on” effects resulting in an interaction between the flow and the structural components within (Chung and Kang, 2003, Barbi et al, 1986).

Within the class of purely oscillatory flows, by far the most studied geometrical configurations were flows past circular cylinders (Obasaju et al., 1988; Iliadis and Anagnostopoulos, 1998) although other geometries have been considered including a square cross-section (inclined at various angles to the flow) or a flat plate perpendicular to the flow (Bearman et al., 1985, Okajima et al., 1997) and triangular and T-shaped geometries (Al-Asmi and Castro, 1992). Other studies investigated the effects of the proximity of the external boundaries on the flow (Sumer et al. 1991). As well as “external” flows, “internal” oscillatory flows have been investigated. These include oscillatory flows in pipes with “wavy” walls (Ralph, 1986), internally placed orifices (De Bernardinis et al., 1981) or internally baffled channels (Roberts and Mackley, 1996).

It is widely accepted that the morphology of the flow structures present within oscillatory flows is governed by three similarity numbers: the Reynolds number ( $Re$ ), the Keulegan-Carpenter number ( $KC$ ) and the Stokes number ( $\beta$ ), although only two

---

<sup>1</sup> Corresponding author; Tel: +44 (0) 161 275 4352; Fax: +44 (0) 870 130 7474; E-mail: a.jaworski@manchester.ac.uk

out of these are really independent, as Stokes number can be expressed as the ratio of Reynolds number to KC number. Tatsuno and Bearman (1990) studied the morphology of the flows generated from the oscillatory cylinder as a function of KC and  $\beta$  while similar studies were performed by Okajima et al. (1997) for square cylinders. These have shown a range of flow regimes ranging from fully attached symmetrical pair of vortices through to symmetrical and alternating vortex shedding.

In all of the experimental studies mentioned above, the typical setup includes either the bluff body being oscillated through the stationary fluid, using some form of mechanical drive, or an oscillating incompressible fluid within U-tube type of water tunnel, with the bluff body being held stationary. However, it should be noted that similar flow problems including vortex shedding phenomena also arise in acoustic systems when the level of acoustic excitation is relatively high. These include systems such as pulse tube refrigerators, standing or travelling wave thermoacoustic devices or their components such as jet pumps, Stirling engines and refrigerators and others, where high intensity acoustic wave (or oscillatory flows in general) encounter sudden discontinuities in the cross-section of an acoustic duct.

The initial motivation for the current paper came from the need to understand the behaviour of the flow in a standing wave thermoacoustic device in the vicinity of the so called “thermoacoustic core”. This typically comprises of a stack of parallel plates (thermoacoustic stack) sandwiched between two heat exchangers (often also constructed as a set of shorter but thicker parallel plates with a somewhat larger pitch). The role of the thermoacoustic core is to either produce acoustic power due to the temperature gradient imposed by the heat exchangers or to consume externally supplied acoustic power in order to facilitate heat pumping from cold to hot heat exchanger by virtue of the so-called thermoacoustic effect (Swift, 2002).

In the high-intensity acoustic field, the flow structures at the end of the stack, or the heat exchanger (or in the region in between) are very complex due to the discontinuities of the cross section and the oscillatory nature of the flow. Clearly, the energy transfer taking place within the thermoacoustic core will be affected by “entrance effects”, vortex shedding and generation (or suppression) of turbulence over different parts of the acoustic cycle. The existing models to calculate the performance of the thermoacoustic systems are based on the linear acoustic models (for example DeltaE, as described by Ward and Swift, 2001) with only some corrections being made to account for non-linear acoustics effects such as turbulence. The development of such codes is hindered by the lack of understanding of the fundamental thermal-fluid processes.

Despite being rooted in the area of thermoacoustics, the current investigation should be seen on a more general level, namely the fundamental fluid dynamical processes of interest to a wider audience. This is the reason why the current research covers somewhat larger parameter space than would be expected from the point of view of thermoacoustic stacks alone and covers the range characteristic for finned heat exchangers and possibly beyond.

The experimental studies of the above phenomena in the context of thermoacoustics are very limited. Gopinath and Harder (2000) studied the heat transfer effects from a single circular cylinder placed in an acoustic resonator (with a possible application to thermoacoustic heat exchangers). They identified two flow regimes: the laminar attached flow regime and the less understood regime where the vortex shedding is prevalent with much higher heat transfer coefficients. Blanc-Benon et al. (2003) used PIV measurements to investigate the flow field around and vortex shedding from a stack of parallel plates for relatively low drive ratios 1.0 – 1.5 % and

compared the experimental results to CFD simulations. They have shown the presence of symmetrical vortices, which on their two experimental configurations (“thin” and “thick” plates) took an “elongated” and “concentrated” form, respectively, but never fully detached from the plates. Mao et al. (2005) conducted similar PIV studies using a somewhat larger geometrical arrangement and higher drive ratios (up to 3%) and showed that at higher drive ratios the symmetrical vortices are replaced by alternately shed vortices. The current paper is an extension of this early work by providing more complete experimental data and its more detailed discussion and analysis.

## 2. Experimental apparatus and procedure

The experimental apparatus used in the current study (Figure 1) was discussed in some detail by Marx et al. (2006) and therefore only a brief description is given here. Its main part is a 7.4m long transparent Perspex pipe, with the internal cross-section 134 x 134 mm, and the wall thickness of 8 mm. One end of the pipe (to the left of Fig. 1) is closed by an “end-cap” with a flush mounted pressure transducer. The other end is connected to a relatively large “loudspeaker box” (600 x 600 x 600 mm) through a 0.3 m long pyramidal section to match the change in cross-sectional dimensions. The resonator is filled with air at atmospheric pressure and room temperature. The first mode of operation (quarter-wavelength) has a fundamental frequency  $f = 13.1$  Hz.

The experiments were conducted for two stacks of plates (shown schematically in Fig. 2). The length,  $l$ , of both stacks was 200 mm, while their width was 132 mm (some clearance had to be left between the stack and the internal resonator wall). Stack I comprised of 21 Perspex plates of thickness  $d = 1.1$  mm with the plate-to-plate spacing  $D = 5$  mm. Stack II was made out of eight Perspex plates with  $d = 5$  mm and  $D = 10$  mm. Both stacks were placed in the resonator 4.1 m from the end as schematically shown in Fig. 1. The drive ratio in the experiments was varied by changing the excitation voltage of the loudspeaker and controlled by measuring the amplitude of pressure oscillations recorded by the dynamic pressure transducer mounted inside the end-cap of the resonator (Endevco Model 8510B-2).

Flow field measurements were performed using a PIV system by TSI. The light sheet from a dual Nd:YAG laser enters the resonator perpendicular to its axis, is reflected by a small mirror and becomes parallel to the resonator axis and normal to the surface of the stack plates. The flow is seeded by particles produced by a smoke generator using 50-50% mixture of glycerol and water, with typical droplet diameter in the range 1–10 microns. Images are taken by a 4 mega-pixel camera (TSI POWERVIEW) and post processed using commercial software (TSI INSIGHT). Cross correlation is used and the interrogation window is 16 pixels by 16 pixels.

The flow field measurements are performed at 20 phases within the acoustic cycle (i.e. every  $18^\circ$ ). Therefore an appropriate phase locking mechanism had to be developed. In this study the pressure oscillation measured by the pressure transducer mounted at the end cap was used as a reference. The output signal from the pressure transducer is connected to an “in-house” made pulse generator, which can generate a pulse sequence of the same frequency as the acoustic wave, but with variable time delay from the trigger point. The output of the pulse generator is connected to the synchroniser (TSI LASERPULSE) that controls the timing of the laser action and triggers the frame grabbing of camera. In this way, the captured images can be phase locked relative to the pressure oscillation (and by the same token to the velocity oscillation, which could be verified independently both by PIV and hot wire measurements). Figure 3 illustrates the timing of 20 phases ( $\Phi_1, \Phi_2 \dots \Phi_{20}$ ) within the

cycle, relative to both velocity and the pressure gradient oscillations. For each of the 20 phases, 100 pairs of images were taken to derive the phase-averaged velocity field. The field of view of the PIV images varied from 25mm×25mm to 60mm×60mm, depending on the flow features to be imaged. This corresponds to the resolution of the velocity vector field between 0.10 mm and 0.23 mm.

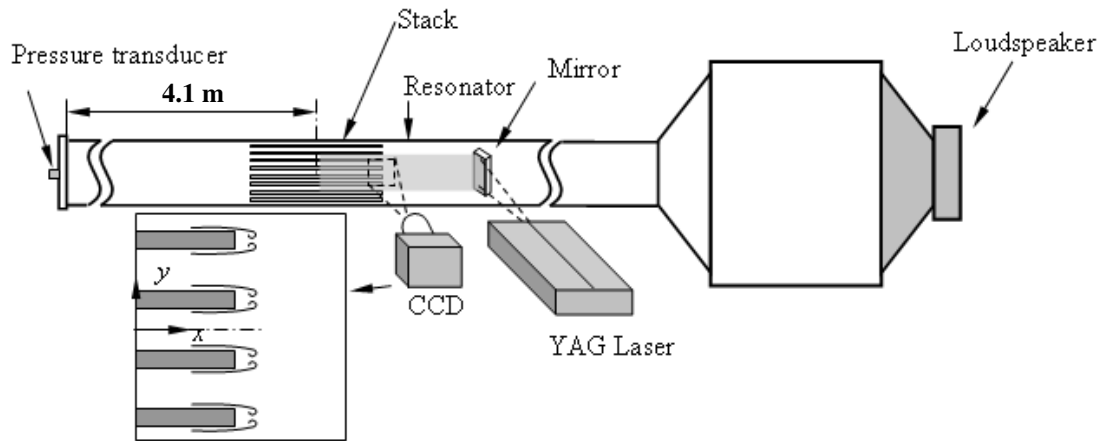


Fig. 1 Sketch of the experimental apparatus

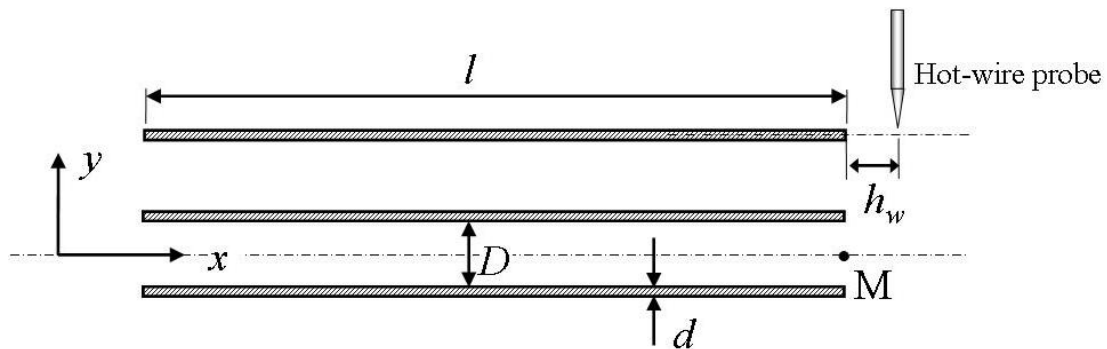


Fig. 2 Geometry of the stack (only three plates shown)

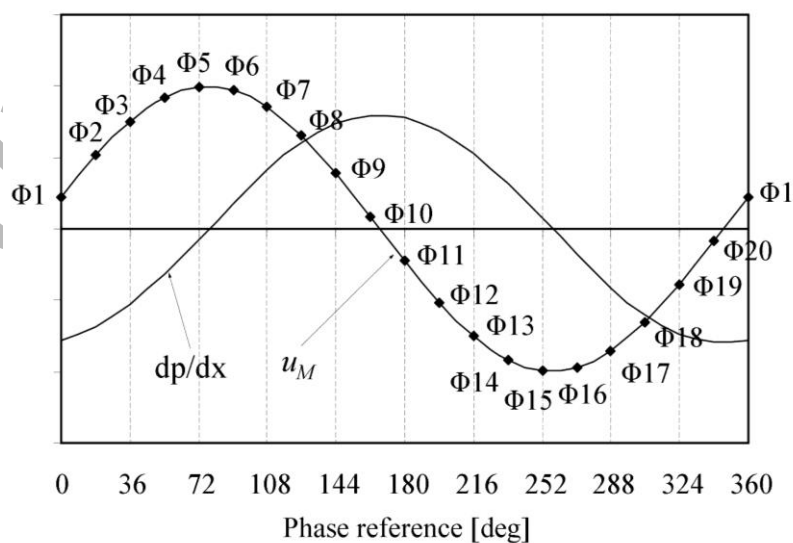


Fig. 3 Phase-averaged velocity oscillation at point M and corresponding phases at which the PIV measurements are taken.  $dp/dx$  is the axial gradient of acoustic pressure in an oscillation period. (Simple-harmonic oscillation is assumed so that  $dp/dx$  is 90 degrees out of phase of velocity oscillation.)

Due to its nature, the PIV technique is not sufficiently “time-resolved” to permit measurements of the fluctuating components of velocity. Therefore the investigations of the vortex shedding frequencies, to be used in estimating typical Strouhal numbers, had to be conducted using standard hot wire methods. Velocity fluctuations were measured with SN type hot-wire probe (DANTEC) operated in the constant-temperature mode using a TSI IFA300 system. The probe is placed normal to the plate, while the sensor is normal to the axis of the resonator. The position of the probe is schematically shown in Fig. 2. For Stack I, the sensor is placed  $2d$  from the edge of the plate, while for Stack II this distance is  $4d$  because the large diameter of the probe support prevents the sensor to be closer to the plate end (the distance from the plate is denoted in Fig. 2 as  $h_w$ ). A high-pass filter set at 30Hz is used to remove the signal component related to the fundamental frequency of 13.1Hz. Both the filtered signal and the unfiltered signal are recorded with a sampling frequency of 5000 Hz. 16384 data points are acquired in a typical experimental condition.

### 3. Experimental results

#### 3.1 Overview of the experimental parameters and conditions

Table 1 summarises the stack dimensions and the basic acoustic excitation and flow conditions. In addition to stack geometry, the table contains porosity,  $\phi$ , defined as the ratio of the total cross-sectional area of the channels within the stack over the cross-sectional area of the resonator. For a stack of evenly spaced plates this can be approximated by  $D/(D+d)$ , assuming that the gaps between the stack and the walls can be neglected. Drive ratio  $D_r$  is the ratio of the acoustic pressure amplitude at the closed end of the resonator,  $p_{1,a}$ , to the mean pressure in the resonator  $p_m$ . The values of the amplitude of the axial velocity,  $u_M$ , at point M (Fig. 2) were extracted from the phase-averaged velocity field for the 20 phases, by using the least square fitting method for a sinusoidal function.  $\xi$  is the displacement amplitude of the oscillating gas parcel. It can be calculated from  $u_M$  as  $\xi = u_M/\omega$ .

The Reynolds number used in the current analysis,  $Re_d$ , is based on the axial velocity amplitude,  $u_M$ , and the plate thickness,  $d$ , as

$$Re_d = \frac{u_M d}{\nu} \quad (1)$$

where  $\nu$  is the kinematic viscosity of air at ambient conditions. However, as will be shown later, for convenience of comparisons between different phases within the cycle it seems useful to introduce a Reynolds number based on the instantaneous value of velocity,  $u_M^*$ , at point M (later referred to as “phase Reynolds number”):

$$Re_d^* = \frac{u_M^* d}{\nu}. \quad (2)$$

Of course,  $u_M^* = u_M \sin(\omega t + \theta)$ , but  $\theta$  could be zero, if one chooses to count the time from the moment when  $u_M^* = 0$ . Similarly, although strictly  $Re_d^*$  can be either positive or negative (depending on the direction of  $u_M^*$ ), it is easy to specify the flow as “out of the stack” and “into the stack” to avoid confusion. Of course, the relationship between the two Reynolds numbers is

$$Re_d^* = Re_d \sin(\omega t + \theta). \quad (3)$$

**Table 1: Summary of stack dimensions and experimental conditions**

	$d$ (mm)	$D$ (mm)	$l$ (mm)	$\phi$	$D_r$ (%)	$u_M$ (m/s)	$\xi$ (mm)	$Re_d$
Stack I	1.1	5.0	200	0.82	0.3	0.84	10.2	62
					0.6	1.68	20.4	123
					1.0	2.82	34.3	207
					1.5	4.32	52.5	317
					2.0	5.68	69.0	417
Stack II	5.0	10.0	200	0.67	0.3	0.95	11.5	317
					0.6	1.95	23.7	650
					1.0	3.24	39.4	1080
					1.5	5.04	61.2	1680
					2.0	6.90	83.8	2300

It is worth making two comments at this point: Firstly, introducing “phase Reynolds numbers” is not an entirely new idea. Yellin (1966) considered flow transition in pulsatile flows within blood vessels and used an analogue of  $Re_d^*$  defined here. Secondly, as will become clearer in later sections (especially 4.2 and 4.3) Reynolds number cannot be a unique similarity number defining the oscillatory flow behaviour in general. This should be remembered when looking at labelling of the experimental data which is made using Reynolds numbers defined by equations (1) and (2).

### 3.2 Oscillatory flow around the end of the stack

Figure 4 represents a typical example of the flow visualisation obtained in the oscillatory flow near the end of the stack, shown here to illustrate its main features. Here the flow past Stack I was investigated at the drive ratio of 1.0%, giving the Reynolds number  $Re_d = 207$  (other relevant parameters can be found in Table 1). The flow features are visualised by using the phase-averaged vorticity field. For brevity, only nine most characteristic phases are selected out of the 20 phases captured within the cycle. These are shown as a time sequence to illustrate the evolution of the flow structures. The phase Reynolds number,  $Re_d^*$ , is included in the graphs; grey areas indicate the presence of the plates within the imaging domain.

As can be seen from Fig. 4, the flow can be divided into two main stages: the “ejection” stage, when the velocity at point M is toward  $x > 0$  (i.e. for phases  $\Phi 1$ – $\Phi 10$  as illustrated in Fig. 3) and the “suction” phase, when the velocity at point M is toward  $x < 0$  (i.e. for phases  $\Phi 11$ – $\Phi 20$  as illustrated in Fig. 3). As can be seen the generation of coherent structures takes place in the “ejection” stage discussed in Section 3.2.1.

#### 3.2.1 Ejection stage

In general the ejection stage can be further subdivided into two different situations: acceleration stage (phases  $\Phi 1$ – $\Phi 5$ ) and deceleration stage (phases  $\Phi 6$ – $\Phi 10$ ). Several characteristic flow phenomena/patterns can be observed: (A) Formation of a pair of attached symmetric vortices; (B) Elongated vortex structures; (C) Break-up of elongated vortices into an asymmetric “vortex street”; (D) Alternate vortex

shedding from the end of the plate. The details of these characteristic flow patterns are described with reference to Fig. 4 (a-e).

**(A) Formation of a pair of attached symmetric vortices:** The flow in phase  $\Phi 1$  (Fig. 4a) has a positive velocity and starts to accelerate. Based on the instantaneous velocity at point M, the corresponding phase Reynolds number,  $Re_d^*$ , is about 47. A pair of vortex structures is formed at the end the plate. They are symmetrical relative to the centre-line of the plate in the x-y plane. Similarly as in the classic case of the wake behind a plate with a square trailing edge (as found in Bachelor, 2000), a recirculation region is formed at the end of the plate, where the pair of vortices remains attached. In the inner region of the channel formed by two neighbouring plates, there is a pair of shear layers with their vorticity in an opposite direction to the vorticity within the plate boundary layer.

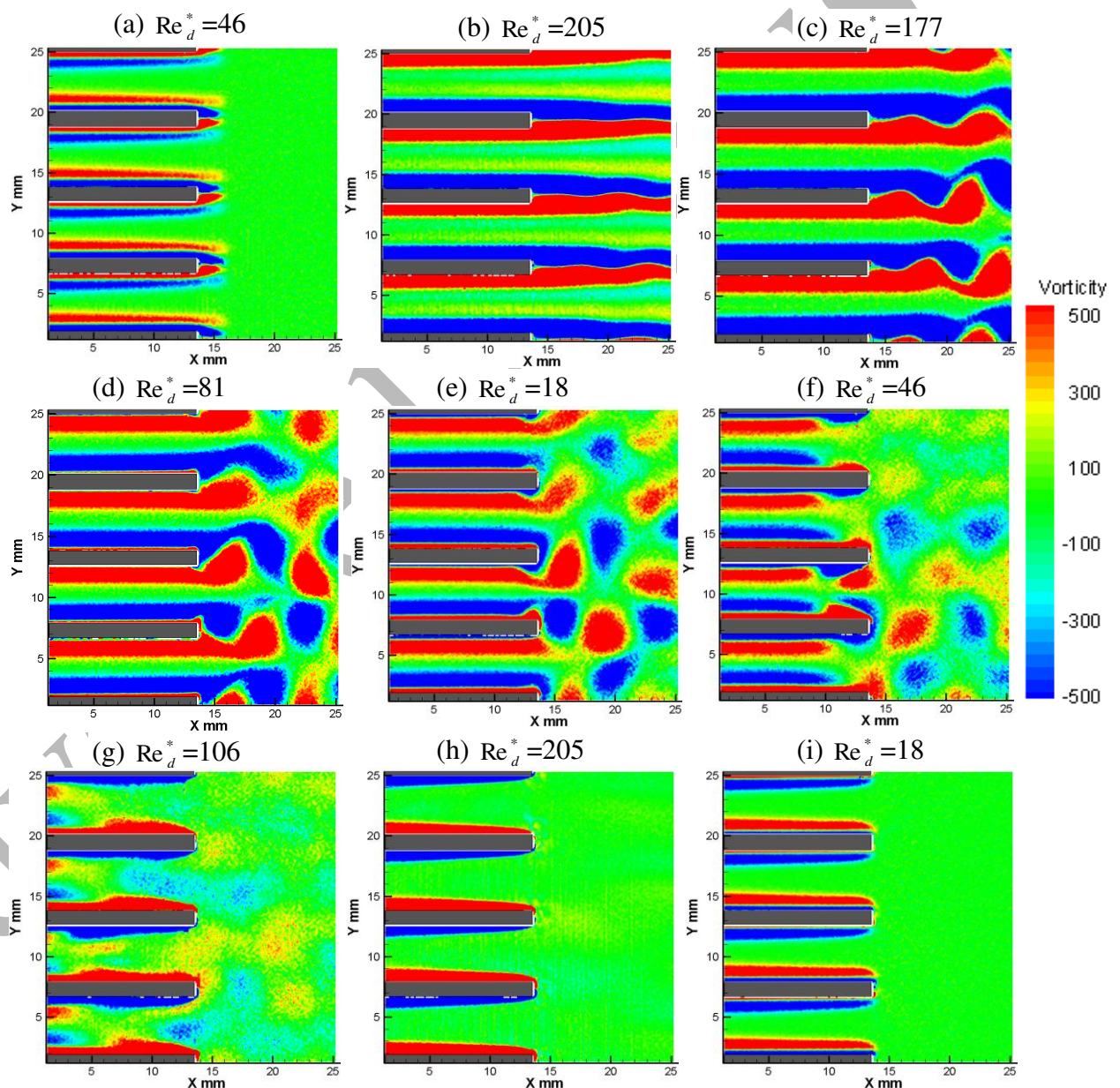


**Figure 4** Vorticity contour map for the flow around the end of Stack I during one acoustic cycle. (a) $\Phi 1$ , (b) $\Phi 5$ , (c) $\Phi 7$ , (d) $\Phi 9$ , (e) $\Phi 10$ , (f) $\Phi 11$ , (g) $\Phi 12$ , (h) $\Phi 15$ , (i) $\Phi 20$  ( $Re_d = 207$ ,  $Dr = 1.0\%$ ). The unit of vorticity legend is  $s^{-1}$

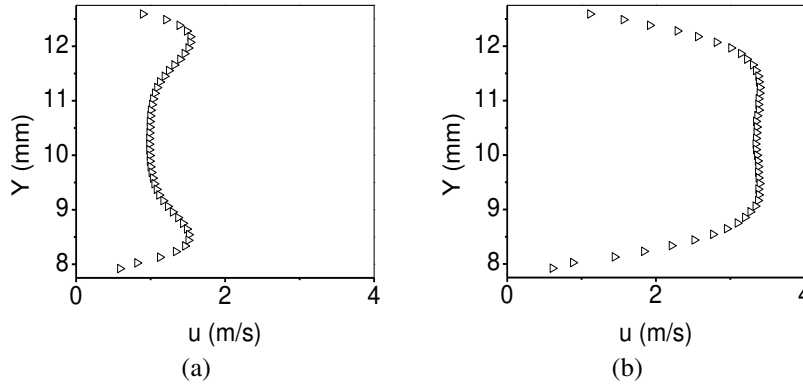


**Figure 5** Transverse profile of axial velocity taken at  $x=5$  mm. Stack I, drive ratio 1%. (a)  $\Phi 1$ , (b)  $\Phi 5$ . (Y remains the same as the coordinate system used in Figure 4)

Such a shear flow pattern exhibited in this phase is directly related to the typical velocity profile shown in Fig. 5a (taken at  $x = 5$  mm according to the coordinate system used in Figure 4). The velocity oscillation of the flow in the central region is delayed in phase, compared with the flow in the boundary layer region. A peak value of velocity appears at some distance from the plate.

**(B) Elongated vortex structures:** As the velocity increases due to the flow acceleration the related phase Reynolds number increases and the flow pattern changes accordingly. At first (during phases  $\Phi 2$ – $\Phi 4$ ) the attached vortex structures remain symmetric but become elongated. However, as the velocity almost reaches its peak around phase  $\Phi 5$ , the very elongated vortex structures in the wake become “asymmetric” by exhibiting somewhat wavy pattern (as shown in Fig. 4b), which seems to be related to the loss of stability in the subsequent phases. The phase Reynolds number  $Re_d^*$  is about 206. Within the channel, the axial velocity profile changes significantly between phases  $\Phi 1$ – $\Phi 5$  by becoming flattened (Fig. 5b). The flow velocity in the central region catches up with the velocity closer to the channel walls, which weakens the vorticity in this central region.

**(C) Break-up of elongated vortices into an asymmetric “vortex street”:** As illustrated in Fig. 3, velocity of the fluid leaving the channels of the stack reaches its maximum between  $\Phi 5$ – $\Phi 6$  and so from then on the fluid enters the deceleration phase. Fig. 4c ( $\Phi 7$ ) shows that the pair of elongated vortex structures has broken up into a “street” of individual vortices in the plate’s wake, very much resembling the classical von Karman street. At phase  $\Phi 7$ , the corresponding phase Reynolds number  $Re_d^*$  is about 177.

**(D) Alternate vortex shedding from the end of the plate:** Once the elongated vortex structures have broken up into the “street” of individual vortices, a different mechanism seems to take over, namely the vortices seem to be shed in an alternating fashion from the end of the plate in a manner resembling the classical bluff body vortex shedding. Figure 4d shows the resulting flow pattern for phase  $\Phi 9$  for the corresponding phase Reynolds number  $Re_d^*$  around 81. The flow slows down even further, and Fig. 4e shows an almost stationary “suspended” vortex pattern just before the flow reverses ( $\Phi 10$ ,  $Re_d^* = 18$ ).

### **3.2.2 Suction stage**

As shown in Fig. 3, the direction of the flow reverses between phase  $\Phi 10$  and  $\Phi 11$ . The fluid and the vortex structures generated in the ejection stage are to be sucked back into the channels between the plates. Figure 4f (phase  $\Phi 11$ ) shows the beginning of such a process. The remains of the vortex street impinge on the end of the plate, the individual vortices becoming split into a series of vortices of much smaller size. The shear layers close to the channel walls are pushed away (displaced) further into the central region of the channel by the continually developing shear layers in an opposite direction – see the channels in Fig. 4f. In addition, in the region near the end of the plate, the entry flow generates a strong shear region, which pushes back (eliminates) the shear layer formed in the ejection stage of the cycle.

In Fig. 4g ( $\Phi 12$ ), the displaced shear layer (which was originally formed in the ejection stage) and the scattered remains of the small vortices finally die out. The newly generated shear layer corresponding to the direction of the suction flow grows and develops.

In Fig. 4h ( $\Phi 15$ ), the negative flow velocity is at its peak value. The unsteadiness of the shear layer still visible in Fig. 4g and the scattered remains of the weak vortices close to the channel centre have disappeared. In general the shear layer next to the surface of the plates is quite similar with the developing boundary layer on a flat plate in the steady flow.

Following phase  $\Phi 15$  the suction flow starts to decelerate and the negative velocity approaches zero at about  $\Phi 20$  (see Fig. 4i). The flow direction is about to change, when the flow enters the ejection stage of the next cycle.

### **3.3 Comparisons between flows at various peak Reynolds numbers, $Re_d$**

To gain further insight into the Reynolds number effects on the flow structure, the flow around the end of the stack was studied at four more drive ratios (0.3, 0.6, 1.5 and 2.0%). In this section, the discussion will focus on the flow structures in the ejecting stages for varying drive ratios.

To save space, the PIV results are shown for a single plate, not an array of plates as previously shown in Fig. 4. Figure 6 shows the flow visualisations for five drive ratios studied (Fig. 6a through to 6e), however instead of using drive ratios, the figures are labelled with the values of Reynolds number,  $Re_d$ , which is more meaningful from fluid mechanics point of view. In each of the figures, the images for five selected phases are shown:  $\Phi 2$ ,  $\Phi 4$ ,  $\Phi 6$ ,  $\Phi 7$  and  $\Phi 9$ , each image also being labelled with the value of the phase Reynolds number -  $Re_d^*$ .

In the simplest approach, one can compare the evolution of the flow patterns during the ejecting stage for different drive ratios (different  $Re_d$ ) by looking at each column in Fig. 6 (i.e. columns a–e). However, one could also imagine a “flow pattern evolution” by looking at a selected phase in the cycle (for example  $\Phi 4$ ) and comparing the flow patterns for varying drive ratios (i.e.  $Re_d$ ). To do this one would have to inspect each row of Figure 6 (rather than each column). In this way one could try to develop a relationship between the flow patterns and the phase Reynolds number,  $Re_d^*$ .

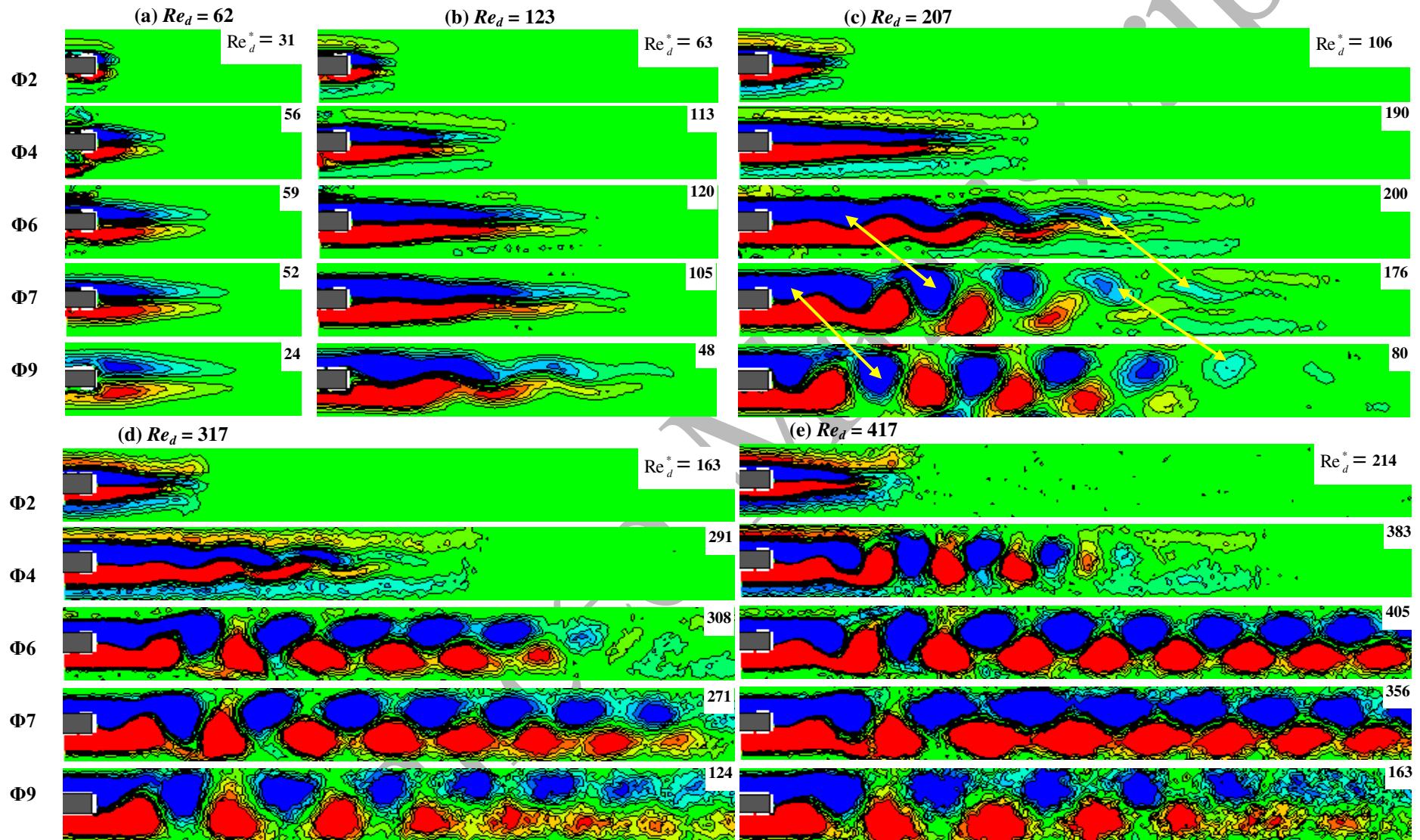


Fig.6 Vorticity field around the end of one plate in Stack I, shown for five drive ratios and five selected phases within the cycle; (a) Dr=0.3%; (b) Dr=0.6%; (c) Dr=1.0%; (d) Dr=1.5%; (e) Dr=2.0%; colour scale is the same as for Figure 4.

Figure 6a shows the results at drive ratio 0.3% ( $Re_d = 62$ ). It can be seen that a pair of vortex structures remains attached to the end of the plate in each phase and remains symmetric relative to the centre line in all phases. The size and strength of the vortices clearly increases as the phase Reynolds number increases throughout the accelerating stage (see  $\Phi 2$  and  $\Phi 4$ ) and increases further in the decelerating flow up until phases  $\Phi 6$  or  $\Phi 7$ . As the vorticity fed from the plate boundary layer decreases, so does the strength of the vortices (see  $\Phi 9$ ).

Figure 6b shows the results at drive ratio 0.6% ( $Re_d = 123$ ). Compared with the vortex structures in Fig. 6a, the vortices become more and more elongated in the accelerating stage. Eventually (around phase  $\Phi 7$ ), the previously symmetrical structures become wavy and this “instability” amplifies in the deceleration phase (see the asymmetric wavy structure in phase  $\Phi 9$ ).

Figure 6c shows the results at drive ratio 1.0% ( $Re_d = 207$ ). They correspond to the results already shown in Fig. 4. From both figures, one can find that the vortex structure exhibits asymmetry in phase  $\Phi 5$  and  $\Phi 6$ , that is at an earlier phase than in Fig. 6b. The break-up of this wavy pattern into a vortex “street” and subsequent shedding from the plate occurs between phase  $\Phi 7$  and  $\Phi 9$ .

Quite similar results can be seen in Fig. 6d, for drive ratio 1.5% ( $Re_d = 317$ ). The vortex structures become unstable even earlier ( $\Phi 4$ ). Further increase of drive ratio, as illustrated in Fig. 6e (2.0%,  $Re_d = 417$ ), leads to even earlier break-up of the initial symmetrical structures - by phase  $\Phi 4$  a vortex “street” is already in place).

One could attempt a qualitative analysis by comparing images in Fig. 6 “row by row”; that is by looking at increasing drive ratios for a fixed phase. For example, the first row of figures shows phase  $\Phi 2$ . From Fig. 6a to Fig. 6e the phase Reynolds number increases from 31 to 214. One can find that, the attached pair of vortices elongates, but remains symmetric as the phase Reynolds number increases.

The second row of figures shows the “flow behaviour” for phase  $\Phi 4$ , as the phase Reynolds number increases from 56 to 383. One can clearly see an “evolution” of the flow patterns similar to phase-by-phase evolution: a pair of symmetric vortices (6a/ $\Phi 4$ ), elongated symmetric vortices (6b/ $\Phi 4$  and 6c/ $\Phi 4$ ) unstable/wavy elongated structure (6d/ $\Phi 4$ ) and alternate vortex shedding (6e/ $\Phi 4$ ).

The third, fourth and fifth rows show the flow pattern “evolution” for phases  $\Phi 6$ ,  $\Phi 7$  and  $\Phi 9$ , respectively. Similar trends in the “development” of the flow patterns can be observed. However, clearly, the vortex shedding pattern is present “earlier” when comparing drive ratios left to right.

### 3.4 Comparisons between flows around Stack I and Stack II

Similar experiments to those described with reference to Stack I were carried out for the second configuration: Stack II (see Table 1 for details). The main reason for selecting this configuration was a further increase in the Reynolds number ( $Re_d$ ) and a change in the porosity of the stack. The same drive ratios were tested which, given a different porosity, resulted in somewhat modified velocities and displacements. The Reynolds numbers were increased roughly about five-fold.

Figure 7 shows the vorticity field around the end of one plate in Stack II (keeping the convention of Fig. 6, for Stack I). Results at five phases of the ejection stage are presented for the stack at the five drive ratios tested, corresponding to the Reynolds number  $Re_d$  of 317, 650, 1080, 1680 and 2300.

By comparing the flow around the end of plate in Figures 6d and 7a, one can see that the value of  $Re_d$  in both cases is the same: 317. However, instead of an elongated vortex structure which breaks-up into a vortex “street” which was the main feature for Stack 1, Stack II exhibits a different flow structure, namely a fully attached and symmetrical pair of vortices, somewhat similar to what was observed for drive ratio 0.3% on Stack I. However, for Stack II, the pair of vortices is much less elongated in the stream-wise direction (only about  $1d$  in terms of plate thickness).

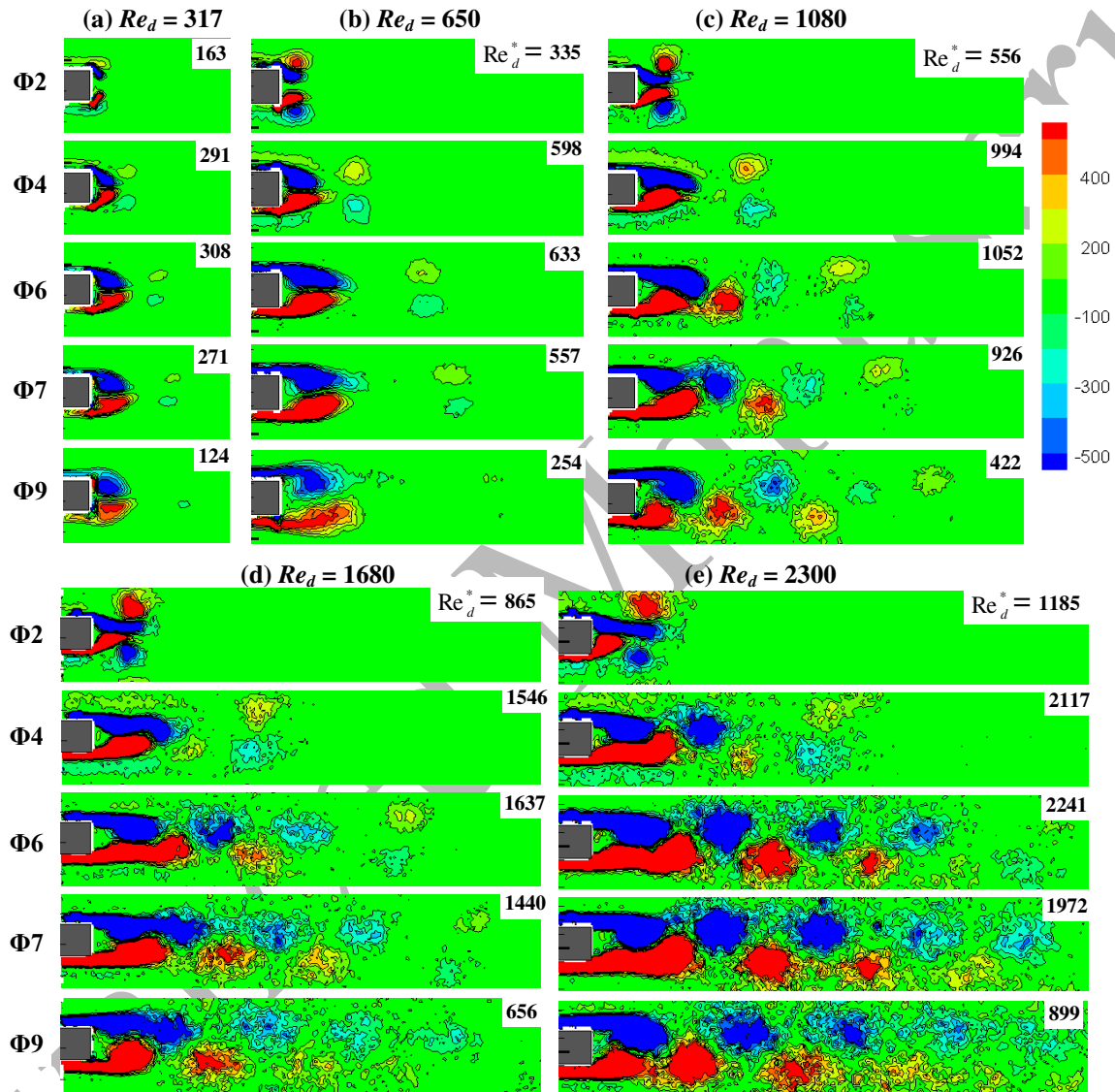


**Fig.7 Vorticity field for the flow around the end of Stack II**  
 (a)  $Dr = 0.3\%$ ; (b)  $Dr = 0.6\%$ ; (c)  $Dr=1.0\%$  (d)  $Dr =1.5\%$  (e)  $Dr = 2.0\%$

Increasing  $Re_d$  to 650 leads to the vortex structures becoming asymmetric (see phase  $\Phi_9$  in Fig. 7b). This feature is more pronounced for  $Re_d = 1080$ - see phases  $\Phi_6$  to  $\Phi_9$  in Fig. 7c. Measurements at even higher drive ratios (Figs. 7d and 7e), show that the higher  $Re_d$ , the earlier in the cycle the asymmetric vortex shedding takes place. It is interesting to note that for Stack II, the two flow patterns at the ejection stage described under (B) and (C) in section 3.2.1 (elongated vortex structures and their break-up) are absent.

Another interesting flow feature is the appearance of a pair of “counter-rotating” vortices, relative to the sense of rotation of the main vortices shed from the plate. The initial formation of these vortices is clearly seen for phase  $\Phi 2$  in Figs. 7a–7e. These “counter-rotating” vortices seem to be convected far away from the plate, preceding the dominating von Karman-type of vortices subsequently shed over the ejection stage of the cycle. By phase  $\Phi 9$ , the vorticity of this pair of “counter rotating” vortices is practically dissipated. These small vortices seem to originate from the remains of the shear layer formed during the suction cycle. Similar feature is indeed present for Stack I, but has a much more elongated shape and is far less “concentrated” in terms of vorticity levels (see for example phase  $\Phi 4$  in Fig. 6d).

In summary, it seems that the main difference in the flow behaviour on two stacks investigated (I and II) is the mode of vortex shedding. While Stack I is dominated by elongated shear layers, which then suddenly break up into a “street” of individual vortices, Stack II exhibits alternate (bluff-body type) shedding very early on within the cycle (as long as the Reynolds number is large enough). This may well be responsible for the differences in Strouhal numbers discussed in Section 3.5.

### 3.5 Frequency of vortex shedding

As illustrated in the previous sections, for both stacks, the vortices will start to shed in an alternate fashion for a sufficiently large Reynolds number,  $Re_d$ . This behaviour is similar to vortex shedding from bluff bodies in steady flows. This part of the study looked at the dependence of vortex shedding frequency (and thus the Strouhal number) on the Reynolds number,  $Re_d$ , and the geometry of the stack. The measurements were performed using standard hot-wire anemometry methods (Section 2) in order to collect the fluctuating velocity signal behind the stack of plates.

Typical signal traces of the hot-wire anemometer output are shown in Figs. 8a and 8c for Stack I and Stack II, respectively. The top signal trace represents the unfiltered signal and the bottom one represents the filtered signal. Each “fluctuation burst” in the bottom signal trace represents an event of vortex shedding in the ejection stage of the acoustic cycle.

The frequency spectrum of the filtered signal trace is analyzed using Fast Fourier Transform (FFT). The signal trace is divided into data blocks, which contain 256 data points, starting at the same phase of an acoustic cycle, and including the whole “fluctuation burst” event. For each block of data, a frequency spectrum is obtained. Subsequently all such frequency spectra, obtained for a given experimental run, are ensemble-averaged and a mean frequency spectrum is obtained. This enables extracting a characteristic peak frequency. Figs. 8b and 8d show the mean frequency spectra of the corresponding signal traces in the left column of Fig. 8. As can be seen from the plots, the curve covers a narrow band of frequencies, as opposed to a sharp spike which would normally be obtained in steady flows past bluff bodies. This is most likely due to variations in the shedding frequency as the instantaneous velocity  $u_M$  changes over the ejection stage, but it may also reflect the fact that vortex shedding is “quasi-periodic” with the pattern changing slightly from cycle to cycle.

The peak frequency is subsequently used to calculate the values of Strouhal number,  $St$  defined here as  $f_{SH} d / u_M$ . Symbol  $f_{SH}$  is used to denote the “shedding frequency” (such as depicted in Fig. 8.) and to distinguish it from the rig’s operating frequency  $f=13.1$  Hz.  $u_M$  is also used to calculate the corresponding values of  $Re_d$ . As shown in Fig.9, for the cases investigated, the Strouhal number is between 0.18

and 0.20 for Stack II, and between 0.08 and 0.10 for Stack I. As already mentioned this difference between the values of the Strouhal number could be related to different phenomena that seem to govern the vortex structure formation: a loss of stability of elongated shear layers for Stack I and bluff-body type of shedding for Stack II.

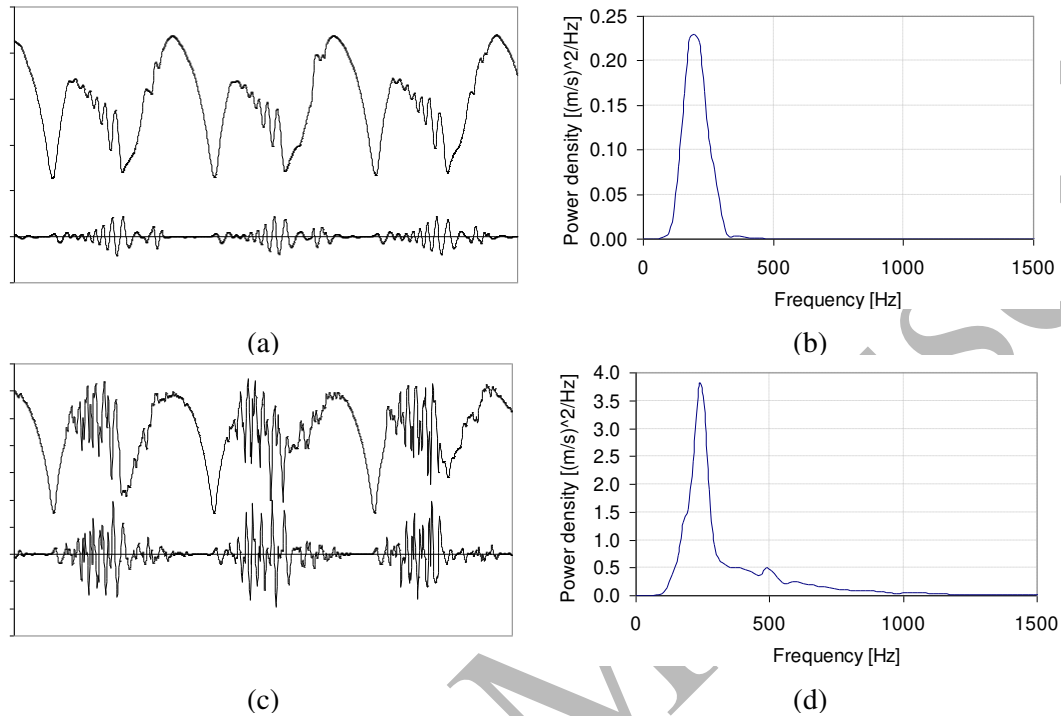


**Fig.8** Signal trace of hot-wire sensor output close to the stack end, and the frequency spectrum of the signal trace; (a, b) Stack I ( $Dr = 1.0\%$ ;  $u_M = 2.7\text{m/s}$ ;  $Re_d = 194$ ); (c, d) Stack II ( $Dr = 2.0\%$ ;  $u_M = 6.5\text{m/s}$ ;  $Re_d = 2165$ )

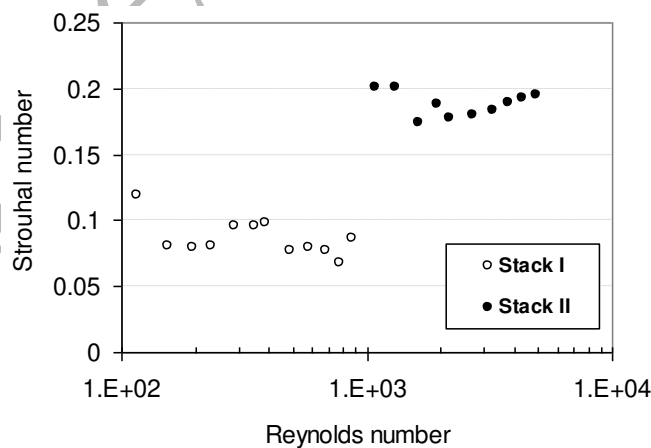


**Fig.9** Strouhal number,  $St$ , versus Reynolds number,  $Re_d$ , based on the plate thickness

#### 4. Discussion of results and direction of further studies

This discussion section highlights some interesting problems in three areas that the current investigation touched upon: the issue of the interaction of the vortex structures originating from adjacent channels with each other, the somewhat

paradoxical issue of the influence of the Reynolds number on the flow patterns for Stack I, and finally the effects of stack geometry. These are discussed in the three sub-sections below.

#### 4.1 “Mirror” vs. “translational” symmetries between adjacent vortex streets

When inspecting the flow patterns generated by the stack of plates such as those shown in Figs. 4d and 4e, it is clear that the resulting vortex “streets” may exhibit either “mirror” or “translational” symmetries in relation to the channels’ centrelines. For example, looking at Fig. 4d, and counting the channels from the bottom of the graph, it is clear that for the first and second channel, the vortex streets have “mirror” symmetries, relative to the channel centre-line. However, for the third channel the symmetry is “translational” (or there is an “anti-symmetry”) in that the vortex pattern shed from the third plate could be overlapped with the vortex pattern shed from the fourth plate if the image was simply shifted upwards. It should be noted that similar problems are encountered in the steady flows past an array of plates (e.g. Guillaume and LaRue, 2002). The future studies should investigate how the spacing between the plates within the stack influences this kind of symmetrical or anti-symmetrical alignment of vortices, and whether there is some kind of a “lock-on” effect when the plates are sufficiently close to one another. This relates to the question of porosity values addressed in section 4.3.

#### 4.2 Reynolds number paradox

When Fig. 6 is studied “row-by-row”, that is for different drive ratios, but the same phase, one can see that as the phase Reynolds number increases the flow pattern “evolves” through the stages that are described as (A)–(D) in section 3.2.1. The latter pattern (D) occurs at higher phase Reynolds number than patterns (A) – (C). However, when the flow patterns are studied “column-by-column”, that is for different phase Reynolds numbers within the same drive ratio, the relationship between the flow pattern and the phase Reynolds number is somewhat different. For example in Fig. 6c, the flow becomes unstable at  $\Phi 6$  ( $Re_d^* = 200$ ), and the vortex shedding is observed at  $\Phi 7$  ( $Re_d^* = 176$ ) and  $\Phi 9$  ( $Re_d^* = 80$ ). This indicates that the flow pattern that usually corresponds to a high Reynolds at an earlier phase can take place at a lower Reynolds number in the decelerating stage. One can find more examples of this phenomenon in Fig. 6. In Fig. 6e  $Re_d^*$  is 214 at  $\Phi 2$ , and the flow has a pair of elongated symmetric vortex structure. On the other hand, in Fig. 6b,  $Re_d^*$  equals 48 at  $\Phi 9$ , and the flow shows a pair of elongated wavy vortices. This clearly illustrates that the transition between different flow patterns cannot be defined by Reynolds numbers alone.

There are at least two explanations for this flow behaviour (referred to here for brevity as “Reynolds number paradox”). The first factor could be the oscillating pressure gradient. It is well known that a favourable pressure gradient (responsible for the flow acceleration) tends to suppress flow instabilities, while the adverse pressure gradient (responsible for the flow deceleration) tends to amplify them (e.g. Lee and Budwig, 1991). This may explain why the vortex structures represented in Fig. 6c break up into a vortex street after phase  $\Phi 6$ . However, an alternative explanation could be found for the flows with higher Reynolds numbers (e.g. Figs. 6d and 6e, where the break-up occurs in the accelerating phase): namely that the vorticity generated on the surface of the plates is too strong to be convected downstream in the

form of an elongated vortex structure and breaks-up so that the flow may assume a more efficient form (vortex street) to convect the vorticity downstream. It is likely that it is the combination of these two factors that decides on the exact nature of the transition between the flow patterns. These aspects of the flow could be studied by means of a rigorous flow stability analysis, which however is somewhat beyond the scope of the current experimental studies.

### 4.3 Similarity issues – geometry and flow parameters

The geometry of a stack of parallel plates (in the 2D “cross-sectional” sense) can be described by three parameters: the plate thickness,  $d$ , the spacing between plates,  $D$  and the length of plates,  $l$ . In all tests presented here, the displacement amplitude of the oscillating gas parcel,  $\xi$ , is much smaller than the length of the plates  $l$ . Therefore, the effect of the stack length on the flow around the end of the stack can be neglected (Swift, 1988). Furthermore, the stack porosity  $\phi$  can be defined as  $D/(D+d)$ , when the plates of the stack are placed evenly. In this case any two of the three parameters, i.e.  $d$ ,  $D$  and  $\phi$ , can uniquely define the stack geometry.

It is also obvious from the current experimental results that changing the Reynolds number,  $Re_d$ , can drastically change the observed flow patterns. However, a triad of two geometrical parameters and a velocity related parameter (Reynolds number or velocity itself) are not sufficient to define the problem entirely. Indeed a large body of literature related to the oscillatory flows past cylinders (Bearman et al. 1985, Badr et al. 1995, Lin et al. 1996, Iliadis and Anagnostopoulos 1998) suggests that frequency of the forcing flow must appear in the problem description in one form or another. A widely accepted parameter of this kind is Keulegan-Carpenter number (KC), usually defined as (velocity)/(frequency x dimension). It is easy to show that this can be expressed here as the ratio of the displacement amplitude to the thickness of the plate,  $\xi/d$ . Of course  $\xi$  can be calculated from  $u_M$  as  $\xi = u_M/\omega$ , where  $\omega = 2\pi f$  is the angular frequency of the acoustic oscillation.

Unfortunately, the data available in the open literature, related to the geometry discussed in this paper (parallel plates), is rather scarce and thus insufficient to perform meaningful similarity studies. The already mentioned paper by Blanc-Benon et al. (2003) allows extracting two experimental “cases” (which are only for relatively small drive ratios). The current work provides a few more “cases”, but there is no independent data to verify any similarities for larger drive ratios. It is therefore hoped that the current work will motivate other researchers to carry out similar studies in flow rigs of different designs.

**Table 2 Parameters of stack geometry and oscillating flow**

	$d$ (mm)	$D$ (mm)	$l$ (mm)	$\phi$	$D_r$ (%)	$u_M$ (m/s)	$\xi$ (mm)	$Re_d$	KC
Stack I	1.1	5.0	200.0	0.82	0.3	0.84	10.2	62	9.3
Stack II	5.0	10.0	200.0	0.67	0.3	0.95	11.5	317	2.3
Configuration A†	1.0	2.0	25.8	0.67	1.0	1.71	1.4	119	1.4
Configuration B†	0.15	1.0	24.0	0.87	1.5	2.57	2.1	18	14.0

† Data adopted from Blanc-Benon et al. (2003)

Table 2 attempts to compare the experimental parameters between the current study and that of Blanc-Benon et al. (2003) for the situations where the flow visualisations in both studies are relatively similar.

The vorticity field for Stack I and Stack II at the conditions listed in the table is shown in Fig.10 (with superimposed black arrows indicating the velocity vector). Blanc-Benon et al (2003) used slightly different measurement protocol: only 16 phases were measured in an acoustic cycle and the phases were counted and labelled in a somewhat different way.

Figures 10a and 10b show phases  $\Phi 7$  and  $\Phi 9$ , which seem to be closest to phases  $t_0+7T/16$  and  $t_0+9T/16$  in Fig. 3 of the paper by Blanc-Benon et al. (2003), related to the flow patterns for their Configuration B. In both situations one can see “elongated” symmetrical vortex structures.

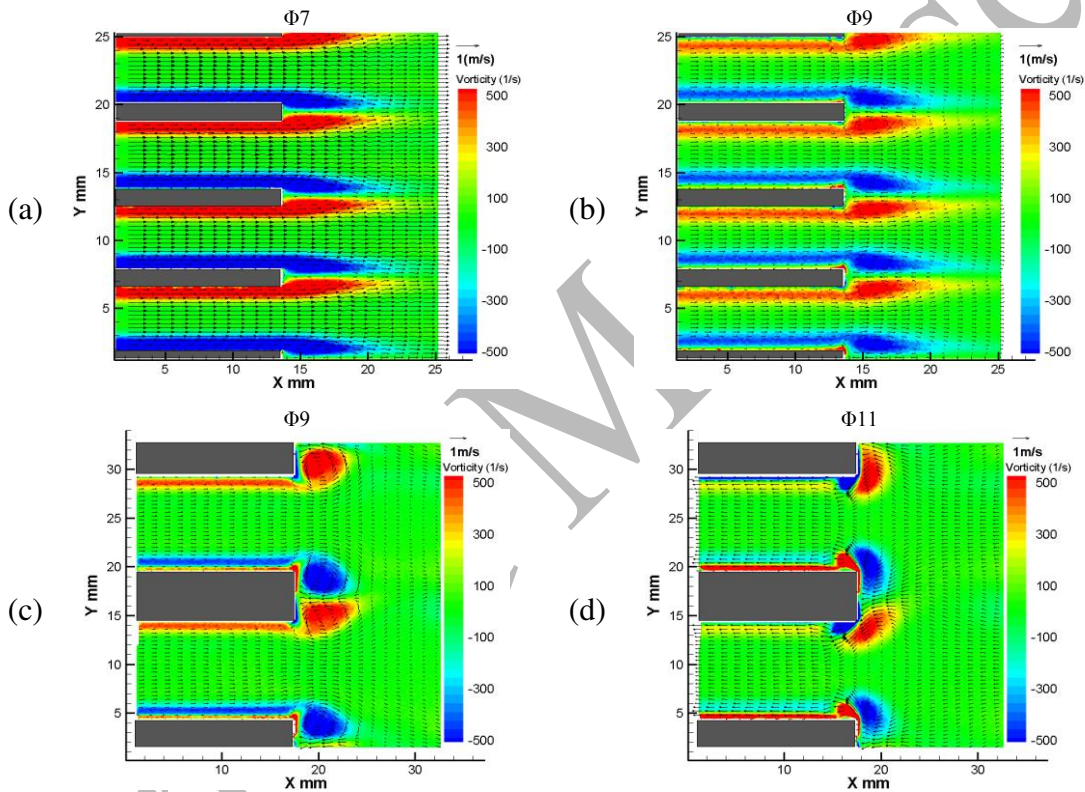


**Fig.10 Vorticity field (contour) and velocity field (vector) of the flow at the stack end. a, b, Stack I ( $Dr=0.3\%$ ); c, d, Stack II ( $Dr=0.3\%$ ).**

Figures 10c and 10d show phases  $\Phi 9$  and  $\Phi 11$ , which seem to be closest to phases  $t_0+T/4$  and  $t_0+3T/8$  in Fig. 2 of the paper by Blanc-Benon et al. (2003), related to the flow patterns for their Configuration A. In both situations one can see more “concentrated” forms of vortices with the length comparable to the plate thickness.

As can be seen from Table 2, KC number has a value of 9.3 for Stack I when the drive ratio,  $Dr$  is 0.3% and 14 for Configuration B. For these two configurations, the vortex structures behind the plates are of a similar elongated form. When the vortex structures are concentrated at the end of plates, such as for Stack II and Configuration A, KC number has a relatively small value of 2.3 for Stack II and 1.4 for Configuration A. Therefore, in addition to the usual choice of the Reynolds number, porosity  $\phi$  and KC number seem to be a promising group of non-dimensional numbers that could be used to describe the effect of the stack geometry on the flow

characteristics when an oscillating flow around the end of a stack of parallel plates is considered. Nevertheless further work would be required (especially in experimenting with different frequencies and characteristic stack dimensions) to extend this kind of comparisons to other flow patterns, especially the alternating shedding that occurs for larger displacement amplitudes.

## 5. Conclusion

In this paper, the flow structures around the end of the stack of parallel plates in the oscillatory flow generated by an acoustic standing wave were investigated using PIV. The flow around two stack configurations was measured for a series of acoustic excitation levels (and thus displacement amplitudes). The resulting flow patterns have been documented and described in some detail. The main findings in this respect are as follows:

1. For the relatively small drive ratios the flow structures already identified by Blanc-Benon et al. (2003) are present within the flow. These include symmetrical and attached pairs of vortices which could be either “elongated” or “concentrated”. However when the drive ratios are increased, other flow patterns exist which lead to alternate type of vortex shedding (similar to von Karman “vortex streets” characteristic for flows past bluff bodies)
2. Two modes of the above mentioned “alternate shedding” were identified on the two stacks considered. The first mode seems to be related to an instability of the elongated shear layers, which leads to their break-up and “fragmentation” into a “vortex street” pattern. The second mode seems to be related to the classical von Karman “vortex street” typically found in bluff body vortex shedding in steady flows. Interestingly, the two different modes seem to lead to two different values of Strouhal number.

Furthermore, the problem of flow “similarities” was addressed, which was discussed in some detail in the context of the “mirror” and “translational” symmetries and the “Reynolds number paradox”, the latter related to the appearance of seemingly similar flow patterns at different phases of the cycle for different drive ratios on Stack I. It is thought that a rigorous stability analysis would be required to explain this flow behaviour.

Finally, the results available in the open literature were compared to some of the results of the current work. The comparison showed that, in order to describe the kind of oscillations investigated here, other non-dimensional parameters should be considered, besides the Reynolds number. In particular, KC number has been pointed out as one possible similarity number. The conclusion that a pair of similarity numbers: Re and KC would be required for characterising oscillatory flows is not surprising given that it is known to appear for oscillatory flows past bluff bodies (e.g. the already mentioned works led by Bearman and Graham). However, the current work essentially deals with periodic structures present in the oscillatory flows. Unfortunately, investigations of such cases are few and far between. Research into the flows past multiple (periodic) bluff bodies are nevertheless available for steady (one-directional) cases (e.g. Auger & Coutanceau 1978, Hayashi et al. 1986, Moretti 1993 and Le Gal et al. 1996). An additional parameter, to just using a Reynolds number, used in such studies is the ratio of pitch-to-diameter. In the present work a similar approach is adopted by introducing porosity,  $\phi$ , as an independent similarity number (notation  $D/(D+d)$  is in effect an inverse of pitch-to-diameter). Therefore, it seems reasonable to suggest that the triad of similarity numbers: Re, KC and  $\phi$  could be

used as a starting point for characterisation of oscillatory flows past periodic structures. Further work to answer some of these important questions is planned.

An interesting point raised by one of the reviewers was related to finding the right scaling parameter for the Strouhal number analysed in section 3.5. In the current work it is based on the plate thickness ( $d$ ), by analogy to bluff body shedding, where typically  $St$  is based on the transverse dimension of the body. The reviewer pointed out that there could be an analogy to jet flows made (the “jet diameter” being the spacing between the plates,  $D$ ). Simple experiments consisting of measuring shedding frequencies for stacks which had every other plate removed did not support the reviewer’s suggestion. Shedding frequency did not scale with  $D$  in the configurations studied. Nevertheless, it is possible to imagine that for certain configurations (e.g. very thick plates separated by narrow gaps) plate spacing may be more appropriate for calculating Strouhal numbers, because there would be very little interaction between adjacent “jets”. Selection of the scaling length is somewhat arbitrary (see for example comments by Moretti 1993 regarding flows past “arrays of tubes”), and often counterintuitive. For example Bunderson and Smith (2005) investigate two planar parallel jets, but derive their Strouhal numbers based on the width of the “centre-body” separating the two jets, not on the width of the jets. Clearly, in the case of oscillatory flows past the series of plates such as described in the current paper, a much larger body of data would be required before one could make a more informed choice regarding the best length scales for non-dimensional studies.

## Acknowledgment

The authors would like to acknowledge the support received from the Engineering and Physical Sciences Research Council (EPSRC), UK and Universities UK.

## References

- Al-Asmi K and Castro IP (1992) Vortex shedding in oscillatory flow: geometrical effects. *Flow Measurement and Instrumentation*, vol. 3, pp 187-202
- Auger JL and Coutanceau J (1978) On the complex structure of the downstream flow of cylindrical tube rows at various spacings, *Mechanics Research Communications*, vol. 5, pp 297-302
- Badr HM, Dennis SCR, Kocabiyik S and Nguyen P (1995) Viscous oscillatory flow about a circular cylinder at small to moderate Strouhal number, *Journal of Fluid Mechanics*, vol. 303, pp 215-232
- Barbi C, Favier DP, Maresca CA and Telionis DP (1986) Vortex shedding and lock-on of a circular cylinder in oscillatory flow, *Journal of Fluid Mechanics*, vol. 170, pp 527-544
- Bachelor GK (2000) *An introduction to fluid dynamics*. Cambridge, Cambridge University Press
- Bearman PW, Downie MJ, Graham JMR and Obasaju ED (1985) Forces on cylinders in viscous oscillatory flow at low Keulegan-Carpenter numbers, *Journal of Fluid Mechanics*, vol. 154, pp 337-356
- Blanc-Benon Ph, Besnoin E and Knio O (2003) Experimental and computational visualization of the flow field in a thermoacoustic stack. *C.R. Mecanique*, vol. 331, pp 17-24
- Bunderson NE and Smith BL (2005) Passive mixing control of plane parallel jets, *Experiments in Fluids*, vol. 39, pp 66-74
- Chung YJ and Kang SH (2003) A study on the vortex shedding and lock-on behind a square cylinder in an oscillatory incoming flow, *JSME International Journal, Series B*, vol. 46, pp 250-261
- De Bernardinis B, Graham JMR and Parker KH (1981) Oscillatory flow around disks and through orifices, *Journal of Fluid Mechanics*, vol. 102, pp 279-299

Gopinath A and Harder DR (2000) An experimental study of heat transfer from a cylinder in low-amplitude zero-mean oscillatory Flows, *International Journal of Heat and Mass Transfer*, vol. 43, pp 505-520

Guillaume DW and LaRue JC (2002) Comparison of the numerical and experimental flowfield downstream of a plate array. *Transactions of the ASME – Journal of Fluids Engineering*, vol. 124, pp 284-286

Hayashi M, Sakurai A and Ohya J (1986): Wake interference of a row of normal flat plates arranged side by side in a uniform flow, *Journal of Fluid Mechanics*, vol. 164, pp 1-25

Iliadis G and Anagnostopoulos P (1998) Viscous oscillatory flow around a circular cylinder at low Keulegan-Carpenter numbers and frequency parameters. *International Journal for Numerical Methods in Fluids*, vol. 26, pp 403-442

Kovaszny LSG (1949) Hot-Wire Investigation of the Wake behind Cylinders at Low Reynolds Numbers, *Proceedings of the Royal Society of London. Series A, Mathematical and Physical Sciences*, vol. 198, No. 1053, pp 174-190

Lee T and Budwig R (1991) The onset and development of circular-cylinder vortex wakes in uniformly accelerating flows, *Journal of Fluid Mechanics*, vol. 232, pp 611-627

Le Gal P, Peschard I, Chauve MP and Takeda Y (1996) Collective behaviour of wakes downstream a row of cylinders, *Physics of Fluids*, vol. 8, pp. 2097-2106

Lin XW, Bearman PW and Graham JMR (1996) A numerical study of oscillatory flow about a circular cylinder for low values of beta parameter. *Journal of Fluids and Structures*, vol. 10, pp 501-526

Mao X, Marx D and Jaworski AJ (2005) PIV measurement of coherent structures and turbulence created by an oscillating flow at the end of a thermoacoustic stack, *Proc. of the iTi Conference in Turbulence, Bad-Zwischenahn, Germany, 25<sup>th</sup>-28<sup>th</sup> September*

Marx D, Mao X and Jaworski AJ (2006) Acoustic coupling between the loudspeaker and the resonator in a standing-wave thermoacoustic device, *Applied Acoustics*, vol. 67, pp 402-419

Moretti PM (1993) Flow induced vibrations in arrays of cylinders, *Annual Reviews in Fluid Mechanics*, vol. 25, pp. 99-114

Obasaju ED, Bearman PW and Graham JMR (1988) A study of forces, circulation and vortex patterns around a circular cylinder in oscillating flow, *Journal of Fluid Mechanics*, vol. 196, pp 467-494

Okajima A, Matsumoto T and Kimura S (1997) Force measurements and flow visualization of bluff bodies in oscillatory flow, *Journal of Wind Engineering and Industrial Aerodynamics*, vol. 69-71, pp. 213-228

Ralph ME (1986) Oscillatory flows in wavy-walled tubes, *Journal of Fluid Mechanics*, vol. 168, pp 518-540

Roberts EPL and Mackley MR (1996) The development of asymmetry and period doubling for oscillatory flow in baffled channels, *Journal of Fluid Mechanics*, vol. 328, pp 19-48

Swift GW (1988) Thermoacoustic engines. *J. Acoust. Soc. Am.* 84: 1145-1180

Swift GW (2002) *Thermoacoustics: A unifying perspective for some engines and refrigerators* (Acoustical Society of America, New York, 2002

Sumer BM, Jensen BL and Fredsbe J (1991) Effect of a plane boundary on oscillatory flow around a circular cylinder, *Journal of Fluid Mechanics* vol. 225, pp 271-300

Tatsuno M and Bearman PW (1990) A visual study of the flow around an oscillating circular cylinder at low Keulegan-Carpenter numbers and low Stokes numbers, *Journal of Fluid Mechanics*, vol. 211, pp. 157-182

Ward B and Swift GW (2001) *Design Environment for Low-Amplitude Thermoacoustic Engines (DeltaE) Tutorial and User's Guide*, Los Alamos National Laboratory

E.L. Yellin (1966) Laminar-Turbulent Transition Process in Pulsatile Flow, *Circulation Research*, vol. 19, pp. 791-804